Stanford Exploration Project, Report 115, May 22, 2004, pages 213–233

Diffraction-focusing migration velocity analysis with application to seismic and GPR data

Paul Sava, Biondo Biondi, and John Etgen[1]

ABSTRACT

We propose a method for estimating interval velocity using the kinematic information in diffractions. We extract velocity information from migrated diffracted events by analyzing their residual focusing in physical space (depth and midpoint) using prestack residual migration. The results of this residual-focusing analysis are fed to a linearized inversion procedure that produces interval velocity updates. Our inversion procedure employs a wavefield-continuation operator linking perturbations of interval velocities to perturbations of migrated images, based on the principles of Wave Equation Migration Velocity Analysis (WEMVA) introduced in recent years. We measure the accuracy of the migration velocity by using a diffraction-focusing criterion, instead of the criterion of flatness of migrated common-image gathers that is commonly employed in Migration Velocity Analysis (MVA). This new criterion enables us to extract velocity information from events that would be challenging to use with conventional MVA methods, and thus makes our method a powerful complement to conventional MVA methods. We demonstrate our method with synthetic and real Ground-Penetrating Radar data.

INTRODUCTION

Migration velocity analysis (MVA) using diffracted events is not a new concept. Harlan (1986) addresses this problem and proposes methods to isolate diffraction events around faults, quantifies focusing using statistical tools, and introduces MVA techniques applicable to simple geology, e.g. constant velocity or $v(z)$. Similarly, de Vries and Berkhout (1984) use the concept of minimum entropy to evaluate diffraction focusing and apply this methodology to MVA, again for the case of simple geology. Soellner and Yang (2002) estimate interval velocities from focusing of diffractions simulated using data-darived parameters.

Sava and Biondi (2004a,b) introduce a method of migration velocity analysis using wave-equation techniques (WEMVA), which aims to improve the quality of migrated images, mainly by correcting moveout inaccuracies of specular energy. WEMVA finds a slowness perturbation which corresponds to an image perturbation. Thus, it is similar to ray-based migration tomography (Al-Yahya, 1989; Stork, 1992; Etgen, 1993), where the slowness perturbation is derived from depth errors, and to wave-equation tomography (Tarantola, 1986; Woodward,

[1]**email:** paul@sep.stanford.edu, biondo@sep.stanford.edu, john.etgen@bp.com

1992; Pratt, 1999; Dahlen et al., 2000) where the slowness perturbation is derived from measured wavefield perturbations.

The moveout information given by the specular energy is not the only information contained by an image migrated with the incorrect slowness. Non-specular diffracted energy is present in the image and clearly indicates slowness inaccuracies. Traveltime-based MVA methods cannot easily deal with the diffraction energy, and are mostly concerned with moveout analysis. In contrast, a difference between an inaccurate image and a perfectly focused target image contains both specular and non-specular energy; therefore WEMVA is naturally able to derive velocity updates based on both these types of information. Our proposed method can benefit, and thus be used in conjunction with, methods to isolate diffracted energy from the seismic data, such as the one proposed by Khaidukov et al. (2004).

In this paper, we use WEMVA to estimate slowness updates based on focusing of diffracted energy using residual migration. One possible application of this technique in seismic imaging concerns areas with abundant, clearly identifiable diffractions. Examples include highly fractured reservoirs, carbonate reservoirs, rough salt bodies and reservoirs with complicated stratigraphic features. Another application is related to imaging of zero-offset Ground-Penetrating Radar (GPR) data, where moveout analysis is simply not an option.

Of particular interest is the case of salt bodies. Diffractions can help estimate more accurate velocities at the top of the salt, particularly in the cases of rough salt bodies. Moreover, diffraction energy may be the most sensitive velocity information we have from under the salt, since most of the reflected energy we record at the surface has only a narrow range of angles of incidence at the reflector, rendering the analysis of moveout ambiguous.

We begin with a summary of the wave-equation MVA methodology, specialized to diffraction focusing, followed by synthetic and real-data examples from seismic and GPR applications.

WEMVA THEORY

In this section, we summarize the main elements of wave-equation migration velocity analysis, by closely following the theory presented in Sava and Biondi (2004a,b). The reader familiar with those details can safely skip to the next section.

We begin with a quick discussion of wavefield scattering in the context of wavefield extrapolation and then define the objective function of our method and the linearized image perturbations which enable us to overcome the limitations of the first-order Born approximation.

Wavefield scattering

Imaging by wavefield extrapolation (WE) is based on recursive continuation of the wavefields ($\mathcal{U}$) from a given depth level to the next, by means of an extrapolation operator (**E**):

$$\mathcal{U}_{z+\Delta z} = \mathbf{E}_z \left[\mathcal{U}_z \right] . \tag{1}$$

Here and hereafter, we use the following notation conventions: $\mathbf{A}\,[x]$ stands for the linear operator **A** applied to x, and $f\,(x)$ stands for function f of argument x.

At any depth z, the wavefield ($\widetilde{\mathcal{U}}$), extrapolated through the background medium characterized by the background velocity ($\tilde{s}$), interacts with medium perturbations (Δs) and creates wavefield perturbations ($\Delta \mathcal{V}$):

$$\Delta \mathcal{V}_z = \mathbf{S}_z \left(\widetilde{\mathcal{U}}_z \right) \left[\Delta s_z \right] . \tag{2}$$

S is a scattering operator relating slowness perturbations to wavefield perturbations. The total wavefield perturbation at depth $z + \Delta z$ is the sum of the perturbation accumulated up to depth z from all depths above ($\Delta \mathcal{U}_z$), plus the scattered wavefield from depth ($\Delta \mathcal{V}_z$) extrapolated one depth step (Δz):

$$\Delta \mathcal{U}_{z+\Delta z} = \mathbf{E}_z \left[\Delta \mathcal{U}_z \right] + \mathbf{E}_z \left[\mathbf{S}_z \left(\widetilde{\mathcal{U}}_z \right) \left[\Delta s_z \right] \right] . \tag{3}$$

We can use the recursive equation (3) to compute a wavefield perturbation, given a precomputed background wavefield and a slowness perturbation. In a more compact notation, we can write equation (3) as follows:

$$\Delta \mathcal{U} = (\mathbf{1} - \mathbf{E})^{-1} \mathbf{E} \mathbf{S} \Delta s , \tag{4}$$

where $\Delta \mathcal{U}$ and Δs stand respectively for the wavefield and slowness perturbations at all depth levels, and **E**, **S** and **1** are respectively the wavefield extrapolation operator, the scattering operator and the identity operator. In our current implementation, **S** refers to a first-order Born scattering operator.

From the wavefield perturbation ($\Delta \mathcal{U}$), we can compute an image perturbation ($\Delta \mathcal{R}$) by applying an imaging condition, $\Delta \mathcal{R} = \mathbf{I} \Delta \mathcal{U}$. For example, the imaging operator, (**I**) can be a simple summation over frequencies. If we accumulate all scattering, extrapolation and imaging into a single operator $\mathbf{L} = \mathbf{I}(\mathbf{1} - \mathbf{E})^{-1} \mathbf{E} \mathbf{S}$, we can write a simple linear expression relating an image perturbation ($\Delta \mathcal{R}$) to a slowness perturbation (Δs):

$$\Delta \mathcal{R} = \mathbf{L} \Delta s . \tag{5}$$

For wave-equation migration velocity analysis, we use equation (5) to estimate a perturbation of the slowness model from a perturbation of the migrated image by minimizing the objective function

$$J\,(\Delta s) = ||\mathbf{W}\,(\Delta \mathcal{R} - \mathbf{L} \Delta s)||^2 , \tag{6}$$

where $\mathbf{W}$ is a weighting operator related to the inverse of the data covariance, indicating the reliability of the data residuals. Since, in most practical cases, the inversion problem is not well conditioned, we need to add constraints on the slowness model via a regularization operator. In these situations, we use the modified objective function

$$J(\Delta s) = ||\mathbf{W}(\Delta\mathcal{R} - \mathbf{L}\Delta s)||^2 + \epsilon^2 ||\mathbf{A}\Delta s||^2 \ . \tag{7}$$

$\mathbf{A}$ can be a regularization operator which penalizes rough features of the model, and ϵ is a scalar parameter which balances the relative importance of the data residual, $\mathbf{W}(\Delta\mathcal{R} - \mathbf{L}\Delta s)$, and the model residual, $(\mathbf{A}\Delta s)$.

An essential element of our velocity analysis method is the image perturbation, $\Delta\mathcal{R}$. For the purposes of the optimization problem in equation (7), this is object is known and has to be precomputed, together with the background wavefield used by the operator $\mathbf{L}$. In the next section, we discuss how $\Delta\mathcal{R}$ is estimated in practice.

Image perturbations

A simple way to define the image perturbation $(\Delta\mathcal{R})$ is to take the image obtained with the background slowness and improve it by applying an image enhancement operator. There are many techniques that can be used to obtain an enhanced image.

- One possibility is to flatten events in angle-domain common-image gathers (ADCIG) by using residual moveout.
- Another possibility is to use residual migration to flatten ADCIGs and, at the same time, focus diffractions which can be observed in common-offset sections.

In principle, both focusing in space (along the midpoint axis) and focusing in offset are velocity indicators, and they should be used together to achieve the highest accuracy. In this paper, however, we emphasize migration velocity analysis using only focusing of diffractions along the spatial axes.

In our current implementation, we use prestack Stolt residual migration (Stolt, 1996; Sava, 2003) as the image enhancement operator ($\mathbf{K}$). This residual migration operator applied to the background image creates new images $(\mathcal{R})$, functions of a scalar parameter (ρ), which represents the ratio of a new slowness model relative to the background one:

$$\mathcal{R} = \mathbf{K}(\rho)[\mathcal{R}_b] \ . \tag{8}$$

We can now take the image perturbation to be the difference between the *improved* image $(\mathcal{R})$ and the *background* image $(\mathcal{R}_b)$:

$$\Delta\mathcal{R} = \mathcal{R} - \mathcal{R}_b \ . \tag{9}$$

The main challenge with this method of constructing image perturbations for WEMVA is that the two images, $\mathcal{R}$ and $\mathcal{R}_b$, can get out of phase, such that they risk violating the requirements

of the first-order Born approximation (Sava and Biondi, 2004a). For example, we might end up subtracting unfocused from focused diffractions at different locations in the image.

We address this challenge by using *linearized image perturbations*. We run residual migration for a large number of parameters ρ and pick at every location the value where the image is best focused. Then we estimate at every point the gradient of the image relative to the ρ parameter and construct the image perturbations using the following relation:

$$\Delta\mathcal{R} \approx \mathbf{K}^{'}\Big|_{\rho=1} [\mathcal{R}_b]\,\Delta\rho\ , \tag{10}$$

where, by definition, $\Delta\rho = 1-\rho$.

The main benefit of constructing image perturbations with equation (10) is that we avoid the danger of subtracting images that are out of phase. In fact, we do not subtract images at all, but we simply construct the image perturbation that corresponds to a particular map of residual migration parameters (ρ). In this way, we honor the information from residual migration, but we are safe relative to the limits of the first-order Born approximation.

Figures 1 and 2 illustrate the migration velocity analysis methodology using residual migration and linearized image perturbations. Figure 1 shows three simple models with diffractors and reflectors with a constant velocity $v = 2000$ m/s. We use these three models to illustrate different situations: an isolated diffractor at location $x = 2000$ m and depth $z = 900$ m, (Figure 1, left), the same diffractor flanked by other diffractors at $z = 1100$ m (Figure 1, middle), and finally the same diffractor next to a short reflector at $z = 1100$ m (Figure 1, right).

We migrate each synthetic datum with an incorrect velocity, $v = 1800$ m/s, and then run residual migration with various velocity ratios from $\rho = 0.7$ to $\rho = 1.1$. From top to bottom, each row corresponds to a different velocity ratio as follows: $0.7, 0.8, 0.9, 1.0, 1.1$. For all residual migration examples, we have eliminated the vertical shift induced by the different velocities, such that only the diffraction component of residual migration is left. Thus, we can better compare focusing of various events without being distracted by their vertical movement.

The images at $\rho = 0.9$ are the best focused images. Since both the backgrounds and the perturbations are constant, the images focus at a single ratio parameter. The ratio difference between the original images at $\rho = 1.0$ and the best focused images at $\rho = 0.9$ is $\Delta\rho = 0.1$. In general, the images focus at different ratios at different locations; therefore $\Delta\rho$ is a spatially variable function.

Using the background images and the measured $\Delta\rho$, we compute the linearized image perturbations (Figure 2, top), and using the WEMVA operator we compute the corresponding slowness perturbations after 15 linear iterations (Figure 2, bottom). The image perturbations closely resemble the background image (Figure 1, fourth row from top), with a $\pi/2$ phase shift and appropriate scaling with the measured $\Delta\rho$.

For all models in Figures 1 and 2, we measure focusing on a single event (the main diffractor at $x = 2000$ m and depth $z = 900$ m), but assign the computed $\Delta\rho$ to other elements of the image in the vicinity of this diffractor. The rationale for doing so is that we can assume that all elements at a particular location are influenced by roughly the same part of the model.

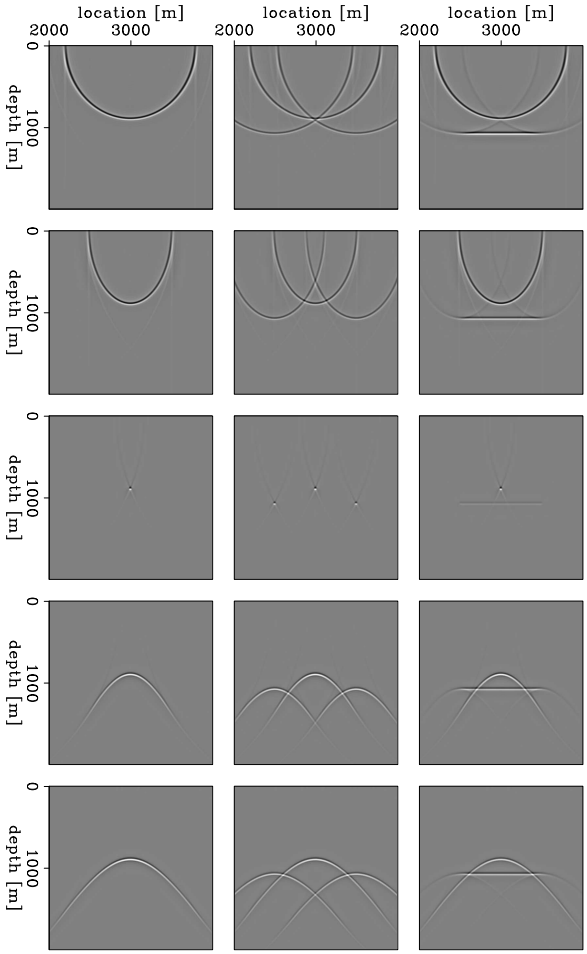

Figure 1: Residual migration applied to three simple synthetic models (from left to right). From top to bottom, the images correspond to the ratios $\rho = 0.7, 0.8, 0.9, 1.0, 1.1$. The middle row corresponds to the correct velocity, when all diffractors are focused. paul2-DIFLAsrm [CR]

Therefore, not only is a priori separation of the diffractors from the reflectors not required, but the additional elements present in the image perturbation add robustness to the inversion.

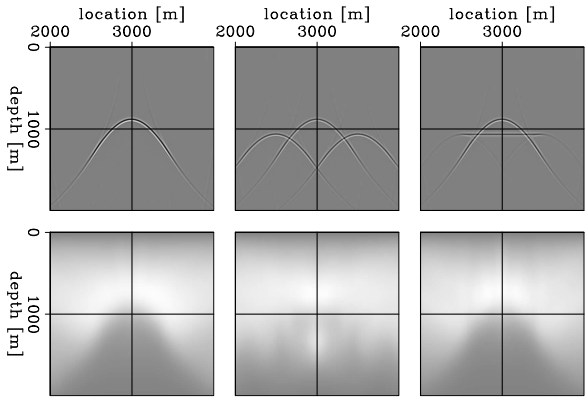

Figure 2: Migration velocity analysis for the three simple synthetic models in Figure 1. The top row depicts image perturbations, and the bottom row depicts slowness perturbations obtained after 15 linear iterations. paul2-DIFLAmva [CR]

EXAMPLES

The first example concerns a synthetic dataset obtained by acoustic finite-difference modeling over a salt body. Although, in this example, we use our technique to constrain the top of the salt, we would like to emphasize that we can use the same technique in any situation where diffractions are available. For example, in sub-salt regions where angular coverage is small, uncollapsed diffractions carry substantial information which is disregarded in typical MVA methodologies.

The second example is a real dataset of single-channel, Ground-Penetrating Radar (GPR) data. Many GPR datasets are single-channel and no method has thus far been developed to estimate a reasonable interval velocity models in the presence of lateral velocity variations. Typically, the velocity estimated by Dix inversion at sparse locations along the survey line is smoothly extrapolated, although this is not even close to optimal from an imaging point of view.

Delineation of rough salt bodies

Figure 3 shows the zero-offset data we use for velocity analysis to delineate the top of the rough salt body. The section contains a large number of diffractors, whose focusing allows us to constrain the overburden velocity model.

Figure 4(a) depicts the starting velocity model, and Figure 4(b) depicts the initial image obtained by zero-offset migration. The starting velocity is a typical Gulf of Mexico $v(z)$ function hanging from the water bottom. Uncollapsed diffractions are visible at the top of the salt, indicating that the velocity in the overburden is not accurate. Such defocusing also hampers our ability to pick accurately the top of the salt and, therefore, degrades imaging at depth.

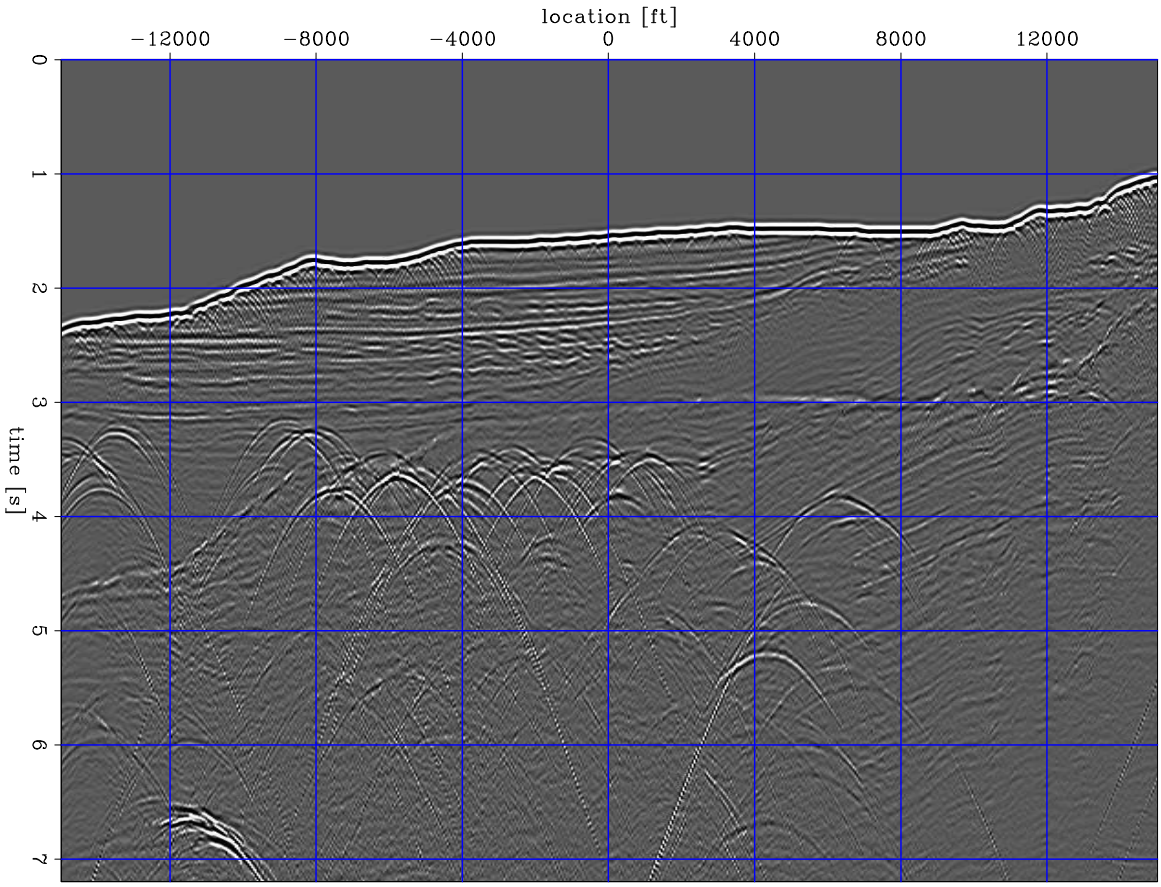

Figure 3: Zero-offset synthetic data used for focusing migration velocity analysis. paul2-BPAITdat [CR]

As we did for the preceding synthetic example, we run residual migration on the background image (Figure 4). Figure 5 shows this image after residual migration with various velocity ratios (Sava, 2003). From top to bottom, the ratios are: $1.04, 1.00, 0.96, 0.92, 0.88$. At $\rho = 1.00$ we recover the initial image. Different parts of the image come into focus at different values of the velocity ratio.

Figure 6(a) shows the picked velocity ratios at various locations in the image. The white background corresponds to picked $\Delta\rho = 0$, and the gray shades correspond to $\Delta\rho$ between 0 and 0.08. Figure 6(b) shows a map of the weights ($\mathbf{W}$) associated to each picked value. The white background corresponds to $\mathbf{W} = 0$, indicating low confidence in the picked values, and the dark regions correspond to $\mathbf{W} = 1$, indicating high confidence in the picked values. In this example, we disregard regions where we did not pick any diffractions. All other regions receive an arbitrary ratio value ($\rho = 1.0$), but also a low weight such that they do not contribute to the inversion. Exceptions include the water bottom, for which we assign a high weight of the picked ratio $\rho = 1.0$, and a few other reflectors for which we did not have any diffraction focusing information.

Figure 7(a) shows the slowness perturbation obtained after 20 iterations of zero-offset

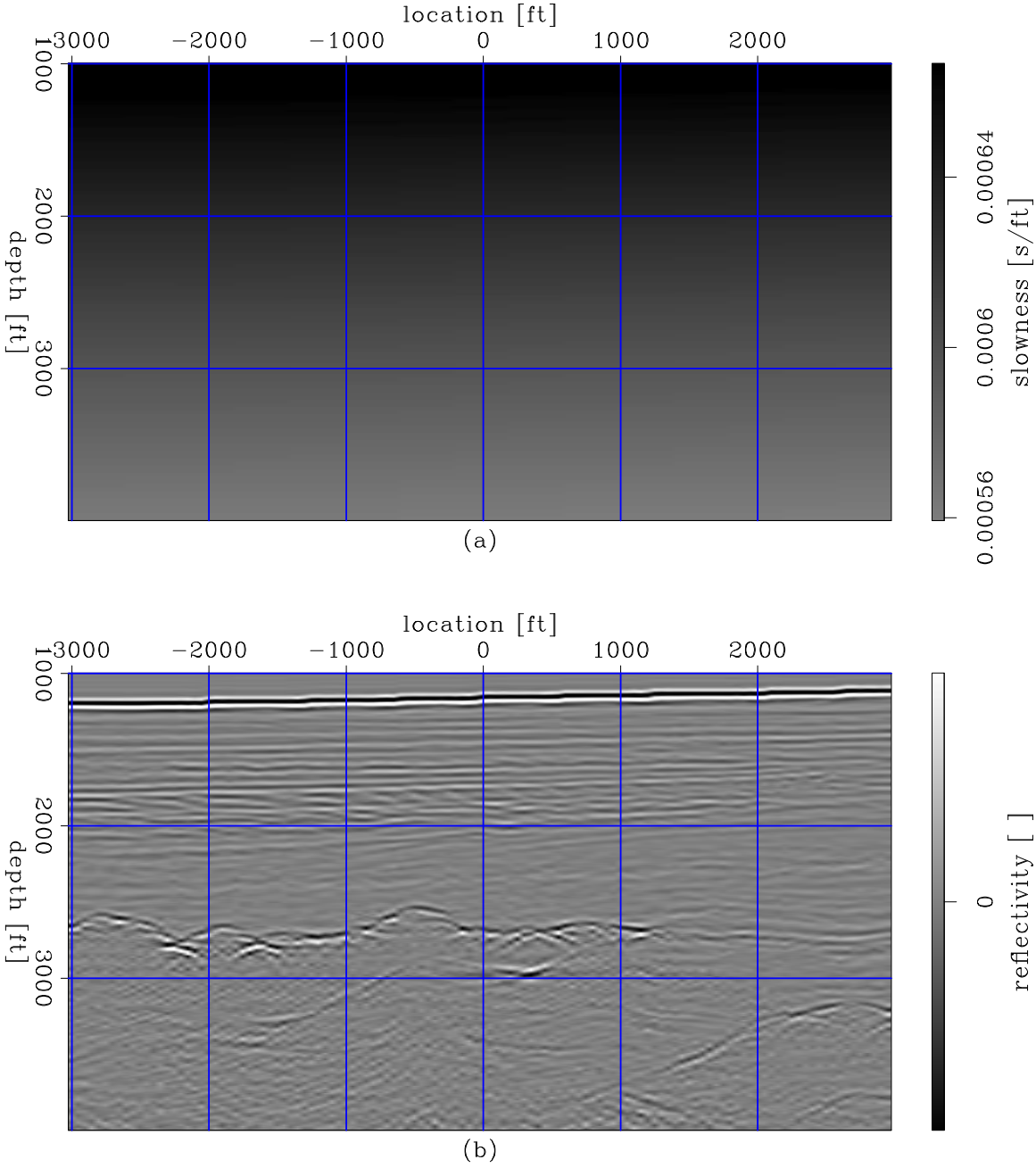

Figure 4: Zero-offset migrated image for the synthetic data in Figure 3: velocity model (a), and migrated image (b). Migration using the initial $v(z)$ velocity model. paul2-BPAITimg1 [CR,M]

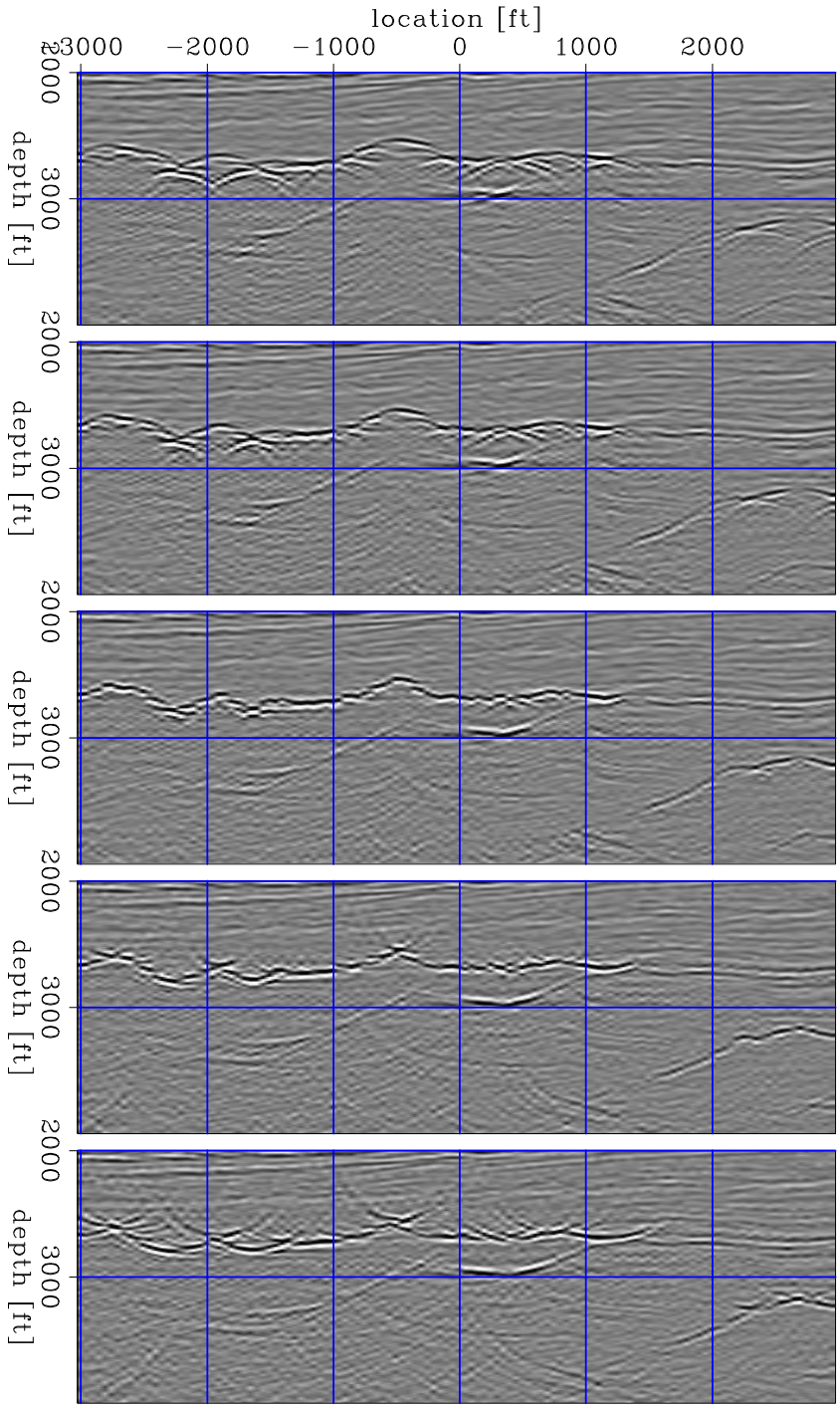

Figure 5: Residual migration applied to the image migrated with the initial velocity model, Figure 4. From top to bottom, the images correspond to the ratios $\rho = 1.04, 1.00, 0.96, 0.92, 0.88$. paul2-BPAITsrm [CR,M]

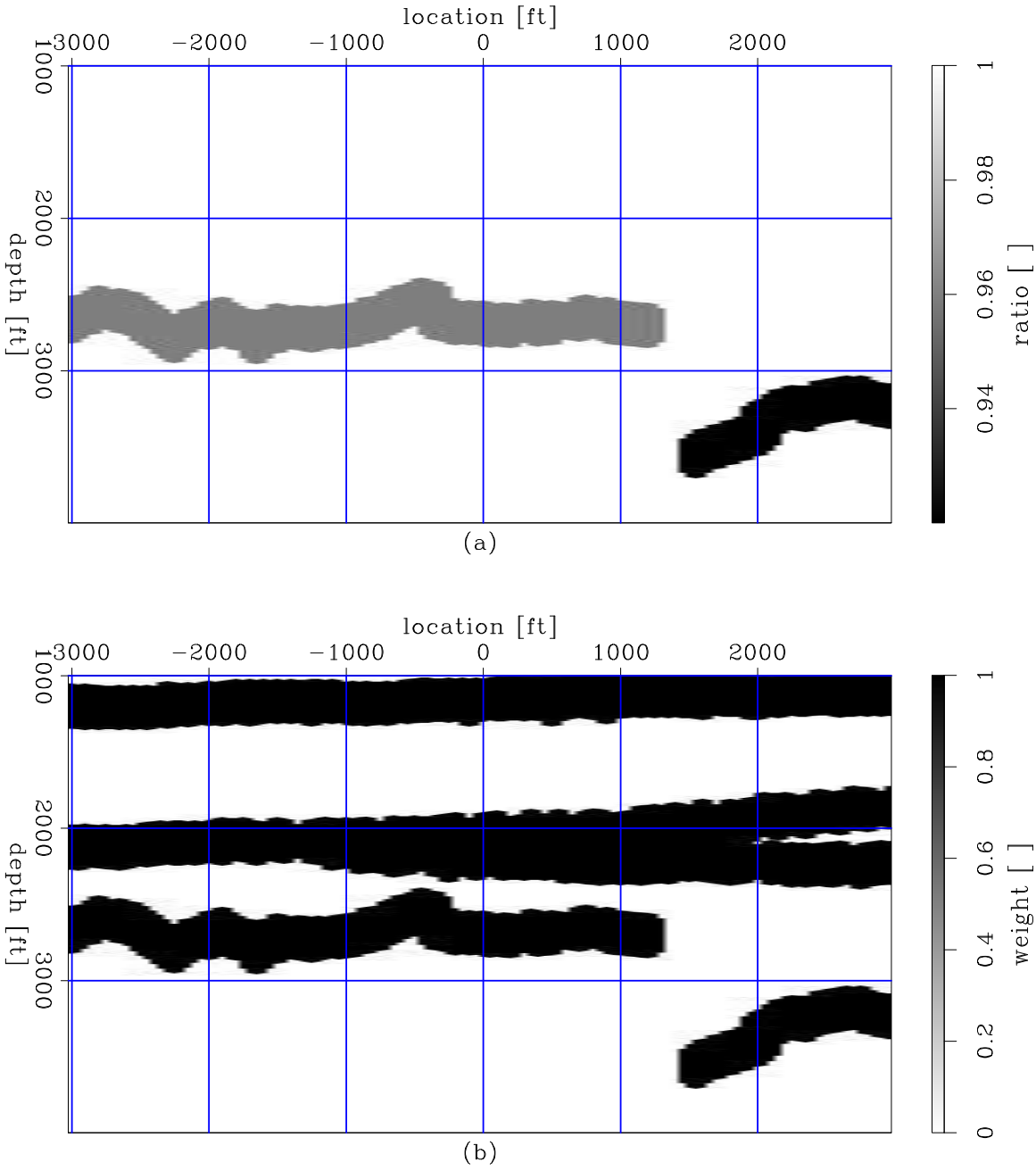

Figure 6: Residual migration picks (a) and the associated confidence weights (b). paul2-BPAITpck [CR,M]

inversion from the image perturbation in Figure 7(b). The image perturbation is non-zero only in the regions where we had diffractions we could pick, as indicated by Figure 6. The smooth slowness perturbation is further constrained by the regularization operator we use, which is a simple Laplacian penalizing the rough portions of the model.

Figure 8(a) shows the updated slowness model and Figure 8(b) shows the zero-offset migrated image corresponding to the updated model. Most of the diffractions at the top of the salt have been collapsed, and the rough top of the salt can be easily picked. The diffractions corresponding to the salt bodies at $x = 2000 - 4000$ ft, $z = 3500$ ft are not fully collapsed, indicating that another nonlinear iteration involving residual migration and picking might be necessary.

Finally, Figure 9 shows prestack migrated images using the initial velocity model (a) and the one updated using zero-offset focusing (b). The top panels depict stacks, and the bottom panels depict angle-domain common-image gathers (ADCIG) (Sava and Fomel, 2003). The ADCIGs show substantial bending after migration with the initial velocity, but they are mostly flat after migration with the updated velocity, although none of the moveout information has been used for velocity update. Figure 10 shows two ADCIGs at $x = -2350$ ft from the images obtained with the initial velocity model (a) and the updated velocity model (b). The ADCIG in panel (a) corresponds to a notch in the top of the salt and is complicated to use for velocity analysis. However, after migration with the updated velocity model, panel (b), the ADCIG is much simpler, and the small residual moveouts can be picked for velocity updates.

A comparison of Figure 8(b) with Figure 9(b) shows a potential limitation of our technique in the presence of prismatic waves (Biondi, 2003). Both images are obtained with the same velocity, the first one with zero-offset data and the second one with prestack data. The imaging artifacts visible at the bottom of the deep canyons at the top of the salt in Figure 8(b) are created by prismatic waves that are not properly imaged from zero-offset data. Prismatic waves are better (though not perfectly) handled by full prestack migration, and thus the artifacts are not visible in the prestack-migrated image shown in Figure 9(b). Since these artifacts resemble uncollapsed diffractions, they may mislead the analysis of the residual migrated images and be interpreted as symptoms of velocity inaccuracies.

Imaging of GPR data

Our next example concerns a zero-offset GPR dataset over a lava flow region. In this situation, diffraction focusing is the only option available for migration velocity analysis. The data depicted in Figure 11 show many diffractions spread over the entire dataset. A few obvious ones are at $x = 22$ ft, $t = 27$ ns, at $x = 28$ ft, $t = 22$ ns, and at $x = 35$ ft, $t = 23$ ns.

We follow the same procedure for migration velocity analysis as the one described for the preceding example. Figure 12(a) shows the initial image obtained by migration with a constant velocity of 0.2 ft/ns, and Figure 12(b) shows the final image obtained after velocity update. We can notice that the image has been vertically compressed, since the velocity update indicated a faster velocity, and most of the diffractions have been collapsed.

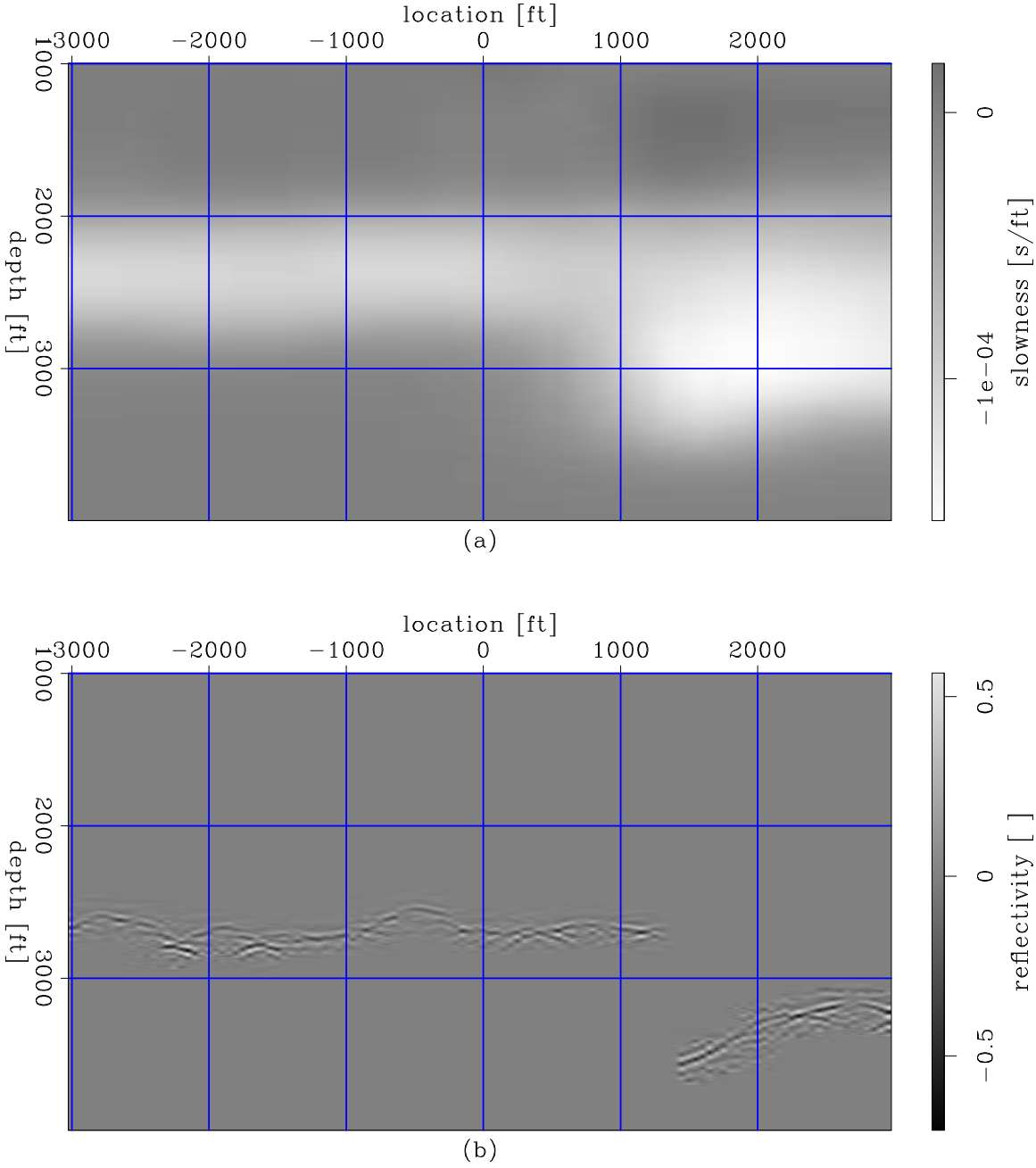

Figure 7: Slowness perturbation (a), derived from an image perturbation (b) derived from the background image in Figure 4 and the velocity ratio picks in Figure 6. paul2-BPAITmva [CR,M]

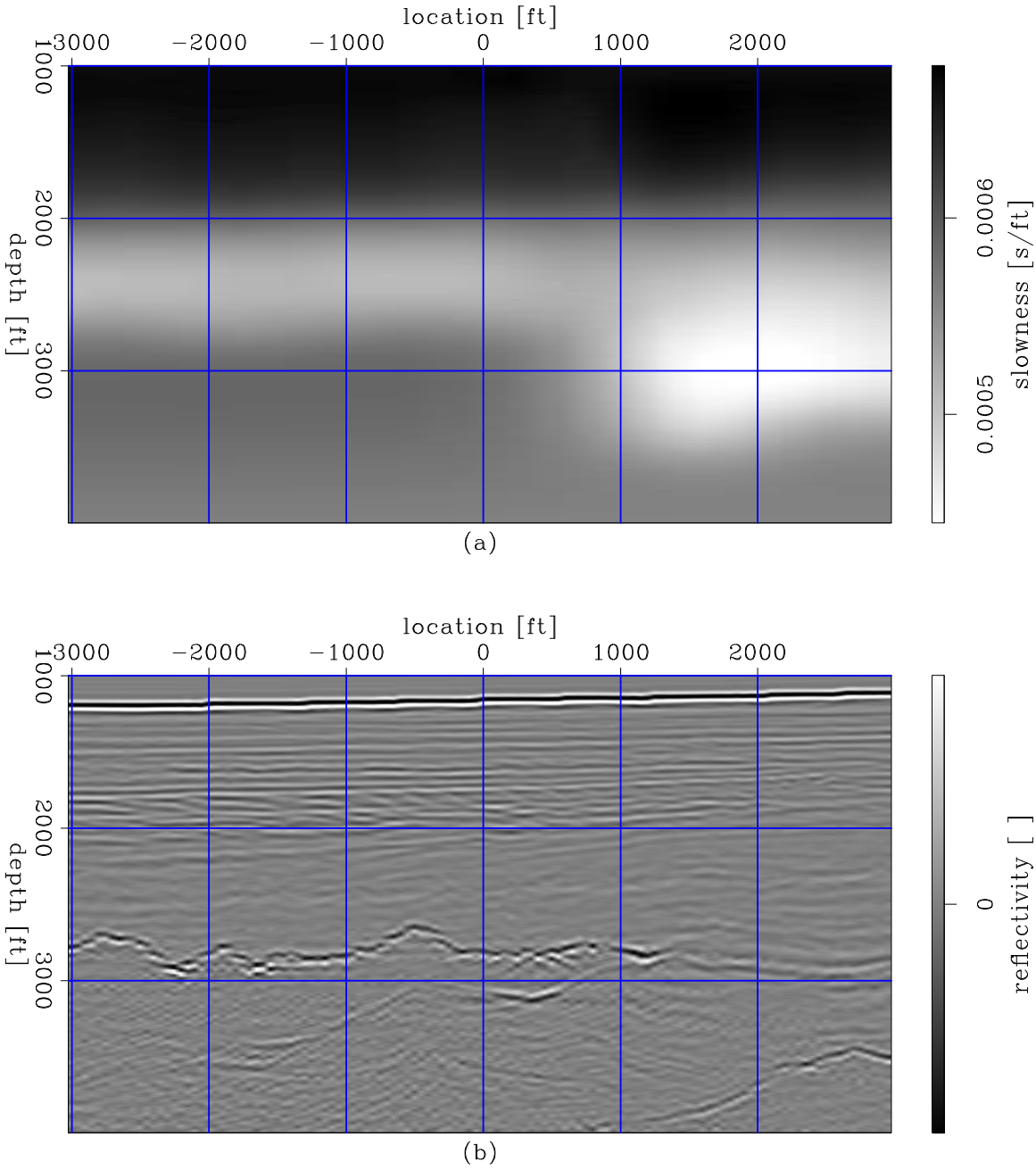

Figure 8: Zero-offset migrated image for the synthetic data in Figure 3: velocity model (a), and migrated image (b). Migration using the updated velocity. paul2-BPAITimg2 [CR,M]

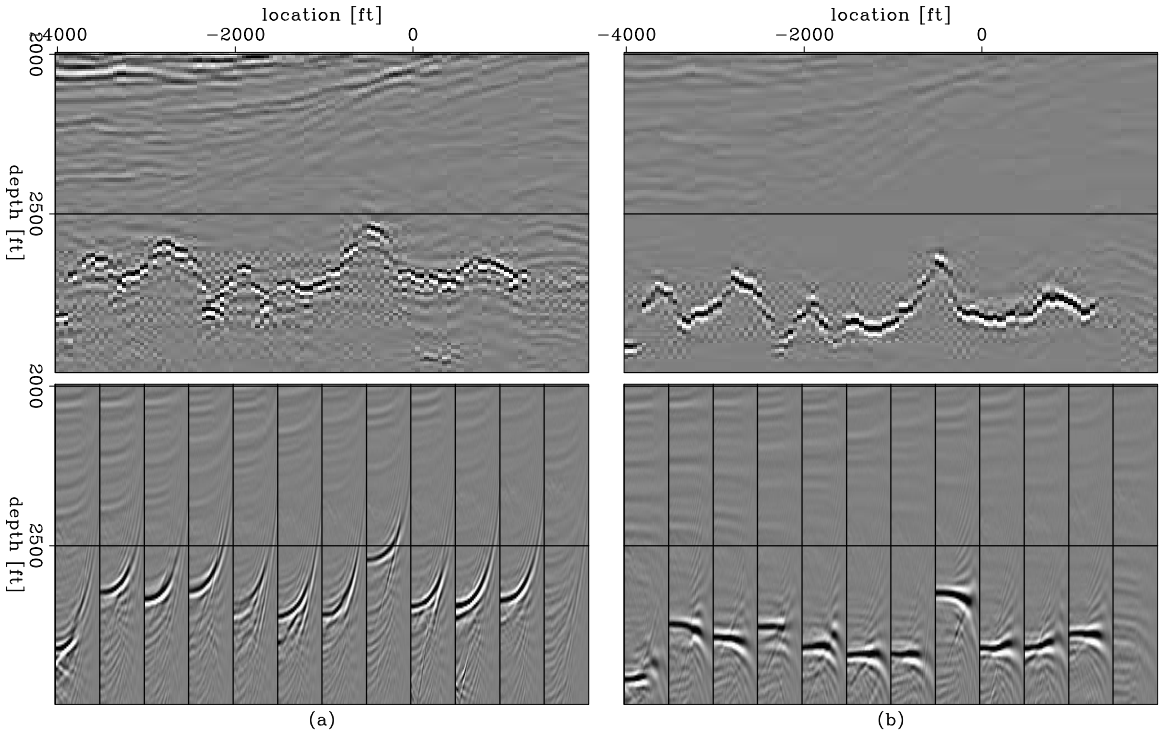

Figure 9: Prestack migrated images using the initial velocity model (a) and the updated velocity model (b). The top panels depict image stacks and the bottom panels depict angle-domain common image gathers. paul2-BPAITpre [CR]

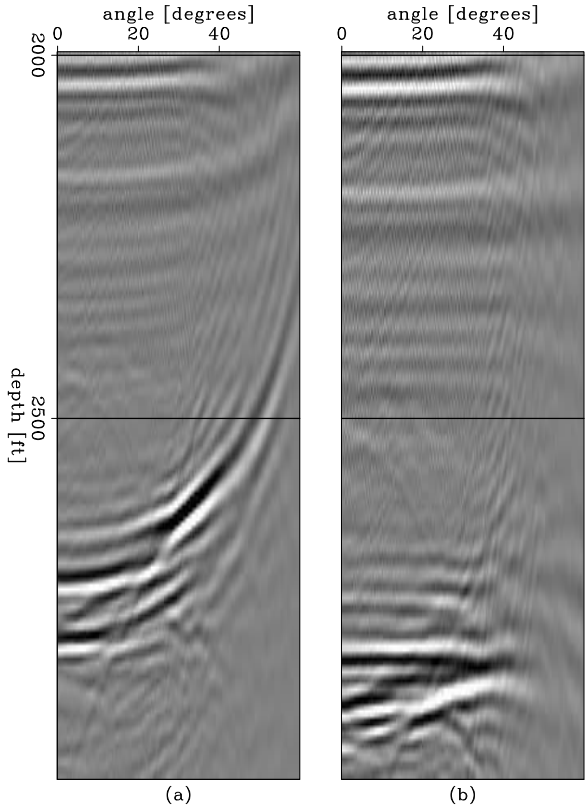

Figure 10: Angle-domain common image gather obtained after migration with the initial velocity model (a) and the updated velocity model (b). paul2-BPAITcig [CR]

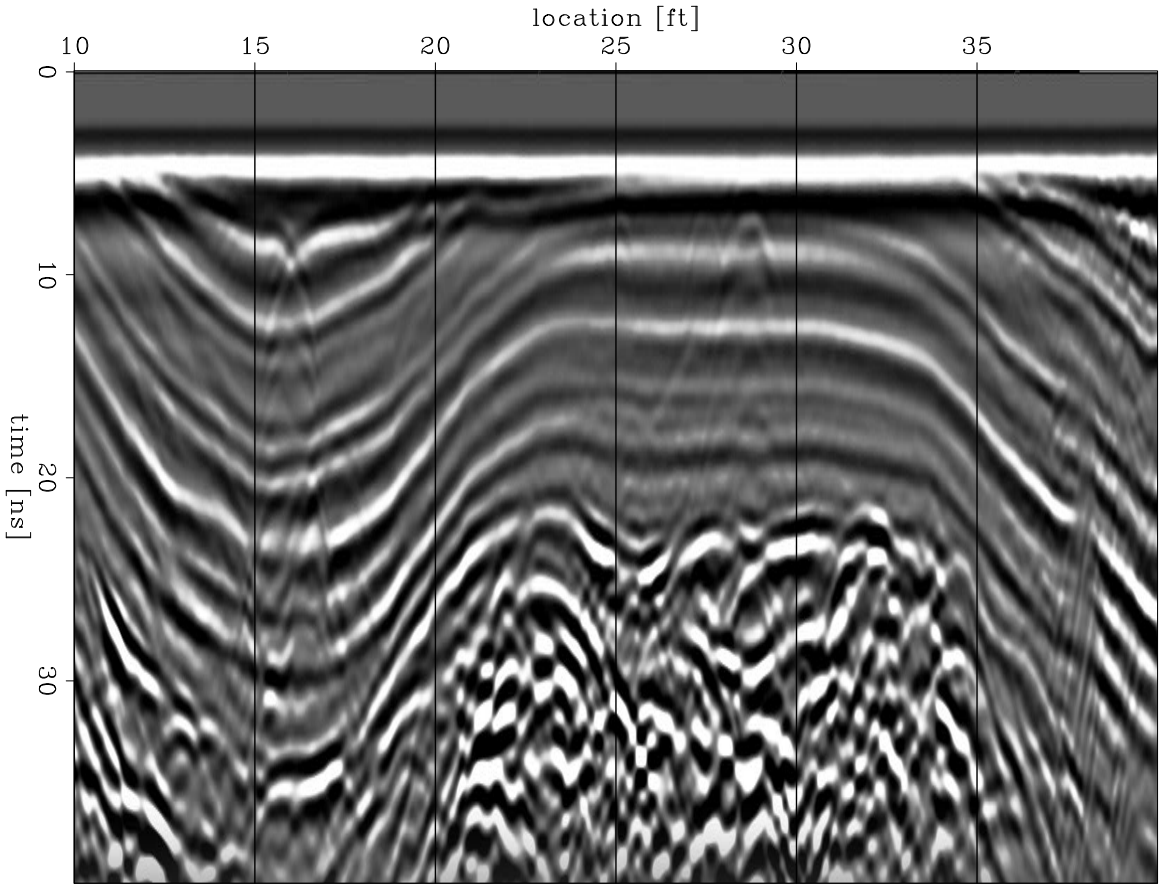

Figure 11: Zero-offset GPR data used for focusing migration velocity analysis. paul2-LAVAdata [CR]

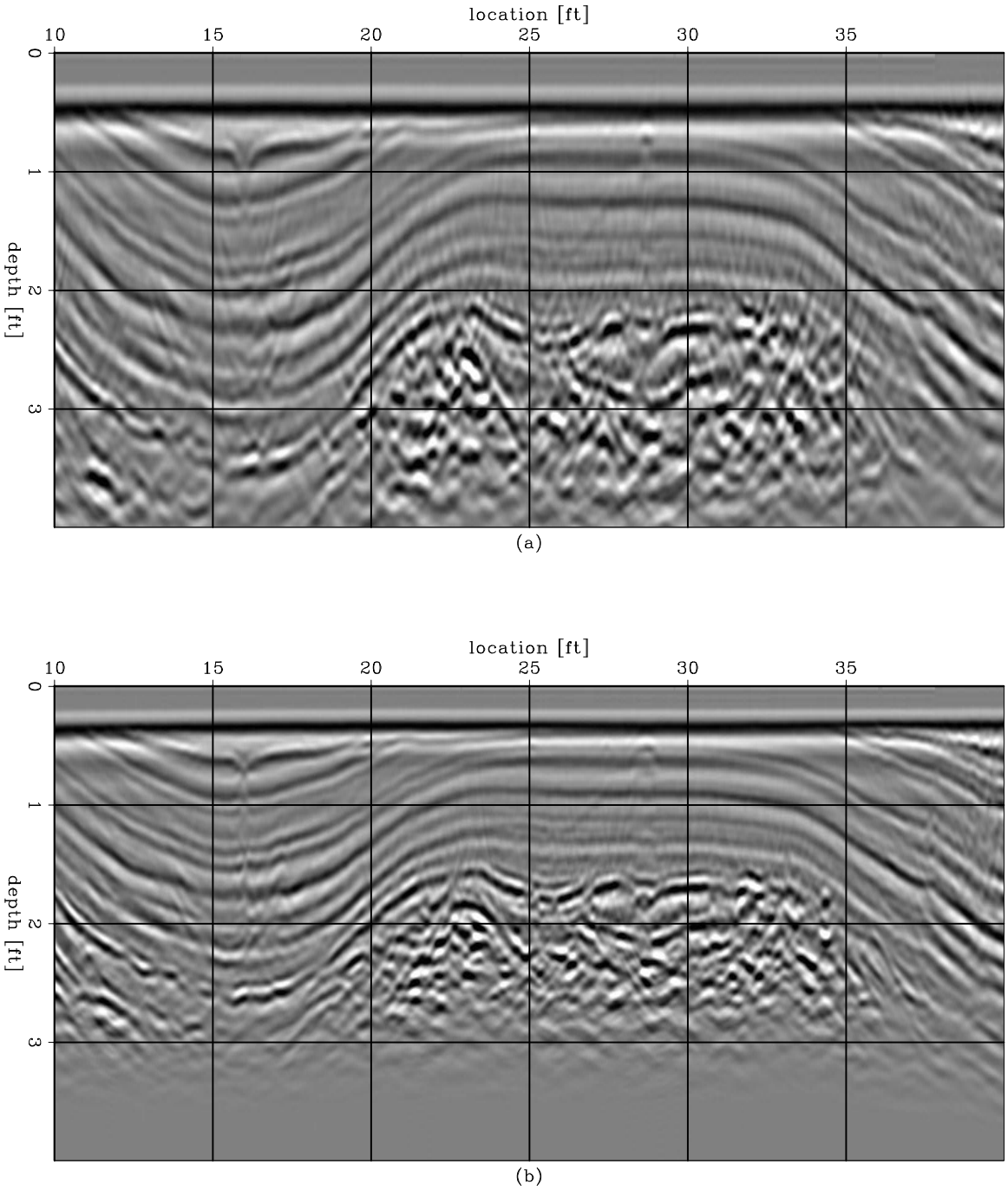

Figure 12: Zero-offset migrated images for the data in Figure 11 using the initial velocity (a) and the updated velocity (b). paul2-LAVAimag [CR,M]

Figures 13 and 14 are detailed views of the initial and final images and slownesses at various locations of interest. Figure 13 shows collapsed diffractions in the left part of the image. We can also observe features with better continuity in the updated image than in the original image, for example at $x = 20-24$ ft and $z = 2$ ft in Figure 13(a,c). Likewise, Figure 14 shows a better focused image than in the original, for example at $x = 34$ ft and $z = 1.8$ ft in Figure 14(a,c).

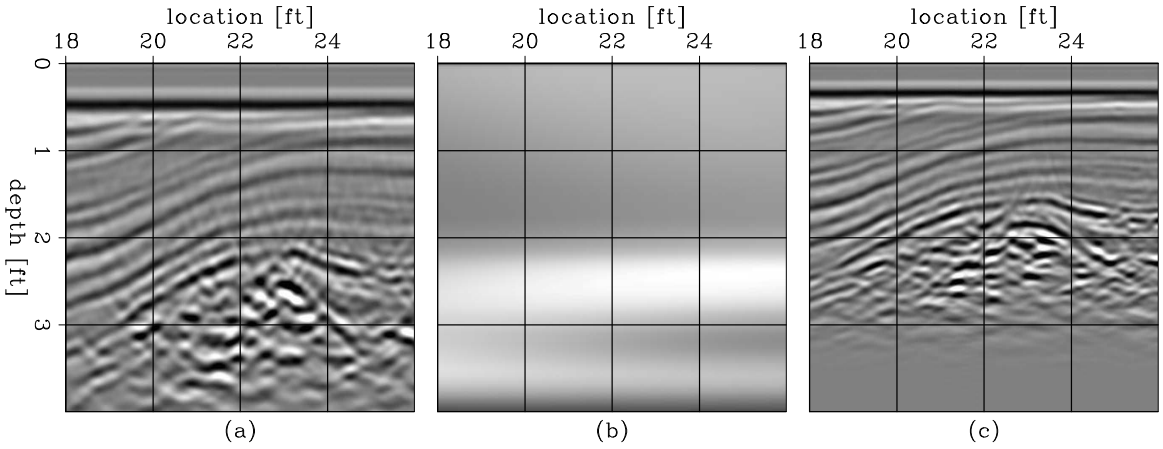

Figure 13: Detail of the images depicted in Figure 12. Migration with the initial velocity (a), updated slowness model (b) and migration with the updated slowness (c). The window corresponds to $x = 20-24$ ft and $z = 2$ ft. paul2-LAVAyoom [CR,M]

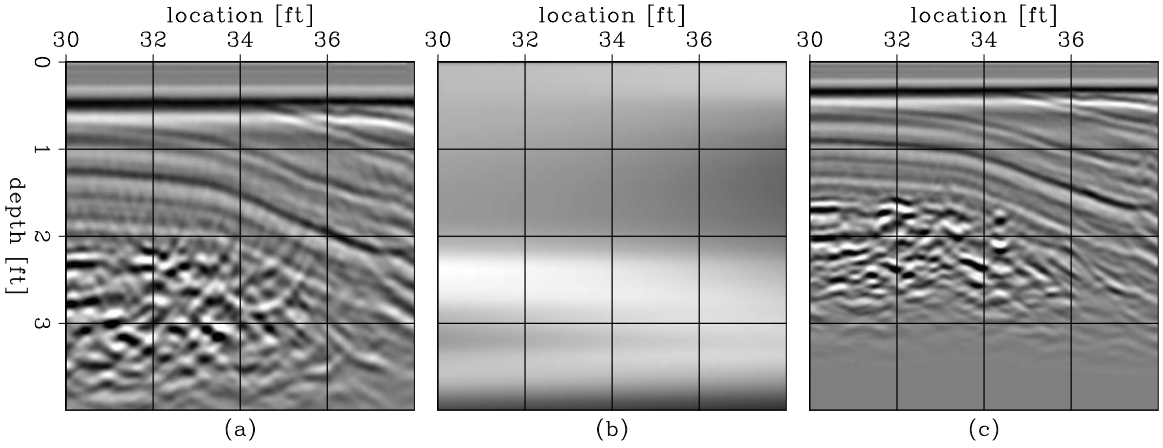

Figure 14: Detail of the images depicted in Figure 12. Migration with the initial velocity (a), updated slowness model (b) and migration with the updated slowness (c). The window corresponds to $x = 34$ ft and $z = 1.8$ ft paul2-LAVAzoom [CR,M]

CONCLUSIONS

Diffracted events contain useful velocity information that is overlooked by conventional MVA methods, which use flatness of common image gathers as the only criterion for the accuracy of migration velocity. In this paper, we demonstrate that accurate interval-velocity updates can be estimated by inverting the results of a residual-focusing analysis of migrated diffracted events. To convert residual-focusing measurements into interval-velocity updates, we employ the WEMVA methodology (Biondi and Sava, 1999; Sava and Fomel, 2002; Sava and Biondi, 2004a,b). Our WEMVA methodology is ideally suited for this task because it is capable of inverting image perturbations directly, without requiring an estimate of the reflector geometry. In contrast, ray-based MVA methods require the reflector geometry to be provided by interpreting the migrated image. However, since the interpretation of partially-focused diffracted events is an extremely difficult task, ray-based methods are never employed for diffraction-focusing velocity analysis.

Our seismic-data example demonstrates how the proposed method can exploit the velocity information contained in the event generated by a rugose salt-sediment interface. This kind of event is present in many salt-related data sets, and the ability of using the diffracted energy to further constrain the velocity model might significantly improve the final imaging results.

The GPR-data example demonstrates the significant potential of our method for improving the imaging of GPR data. We demonstrate that the interval-velocity model obtained by extracting velocity information from the diffracted events improves the reflector continuity in the migrated image and facilitates geological interpretation of the images. Since a large number of GPR data sets are limited to zero-offset data, the possibility of using diffractions to define the lateral variations in interval velocity can substantially widen the range of applications of GPR methods.

ACKNOWLEDGMENTS

We would also like to acknowledge Frederic Billette (BP) for providing the synthetic salt-dome dataset and Antoine Guitton (SEP) for suppressing multiples in this dataset. Kevin Williams of the Smithsonian Institution in Washington, D.C. provided the GPR dataset.

REFERENCES

Al-Yahya, K. M., 1989, Velocity analysis by iterative profile migration: Geophysics, **54**, no. 06, 718–729.

Biondi, B., and Sava, P., 1999, Wave-equation migration velocity analysis: 69th Ann. Internat. Meeting, Soc. of Expl. Geophys., Expanded Abstracts, 1723–1726.

Biondi, B. L., 2003, 3-D Seismic Imaging: `http://sepwww.stanford.edu/sep/biondo/Lectures/index.html`.

Dahlen, F. A., Hung, S. H., and Nolet, G., 2000, Frechet kernels for finite frequency traveltimes—I. Theory: Geophys. J. Int., **141**, 157–174.

de Vries, D., and Berkhout, A. J., 1984, Velocity analysis based on minimum entropy: Geophysics, **49**, no. 12, 2132–2142.

Etgen, J. T., 1993, Interval velocity estimation using residual prestack migration: Soc. of Expl. Geophys., 63rd Ann. Internat. Mtg, 669–672.

Harlan, W. S., 1986, Signal-noise separation and seismic inversion: Ph.D. thesis, Stanford University.

Khaidukov, V., Landa, E., and Moser, T., 2004, Diffraction imaging by focusing-defocusing: an outlook on seismic superresolution: Geophysics, submitted for publication.

Pratt, R. G., 1999, Seismic waveform inversion in the frequency domain, Part 1: Theory and verification in a physical scale model: Geophysics, **64**, no. 3, 888–901.

Sava, P., and Biondi, B., 2004a, Wave-equation migration velocity analysis—I: Theory: Geophysical Prospecting, submitted for publication.

Sava, P., and Biondi, B., 2004b, Wave-equation migration velocity analysis—II: Examples: Geophysical Prospecting, submitted for publication.

Sava, P., and Fomel, S., 2002, Wave-equation migration velocity analysis beyond the Born approximation: 72nd Ann. Internat. Mtg., Soc. of Expl. Geophys., Expanded Abstracts, 2285–2288.

Sava, P., and Fomel, S., 2003, Angle-domain common image gathers by wavefield continuation methods: Geophysics, **68**, no. 3, 1065–1074.

Sava, P., 2003, Prestack residual migration in the frequency domain: Geophysics, **67**, no. 2, 634–640.

Soellner, W., and Yang, W., 2002, Diffraction response simulation: A 3D velocity inversion tool: Soc. of Expl. Geophys., 72nd Ann. Internat. Mtg, 2293–2296.

Stolt, R. H., 1996, Short note - A prestack residual time migration operator: Geophysics, **61**, no. 02, 605–607.

Stork, C., 1992, Reflection tomography in the postmigrated domain: Geophysics, **57**, no. 05, 680–692.

Tarantola, A., 1986, A strategy for nonlinear elastic inversion of seismic reflection data: Geophysics, **51**, no. 10, 1893–1903.

Woodward, M. J., 1992, Wave-equation tomography: Geophysics, **57**, no. 01, 15–26.